frontiers in Environmental Science

ORIGINAL RESEARCH
published: 21 December 2021
doi: 10.3389/fenvs.2021.799264

Removal Study of Crystal Violet and Methylene Blue From Aqueous Solution by Activated Carbon Embedded Zero-Valent Iron: Effect of Reduction Methods

Yongmei Wang[1], *Tiantian Chen*[2]*, *Xiaolin Zhang*[3] *and Teza Mwamulima*[3]

[1]College of Safety and Environmental Engineering, Shandong University of Science and Technology, Qingdao, China, [2]CAS Key Laboratory of Marine Ecology and Environmental Sciences, Institute of Oceanology, Chinese Academy of Sciences, Qingdao, China, [3]College of Environmental Science and Engineering, Ocean University of China, Qingdao, China

OPEN ACCESS

Edited by:
Lean Zhou,
Changsha University of Science and Technology, China

Reviewed by:
Rui Hou,
South China Sea Institute of Oceanology (CAS), China
Hongliang Li,
Taiyuan University of Technology, China
Jingju Cai,
Central South University of Forestry and Technology, China

***Correspondence:**
Tiantian Chen
chentian0819@163.com

Specialty section:
This article was submitted to Water and Wastewater Management, a section of the journal Frontiers in Environmental Science

Received: 21 October 2021
Accepted: 25 November 2021
Published: 21 December 2021

Citation:
Wang Y, Chen T, Zhang X and Mwamulima T (2021) Removal Study of Crystal Violet and Methylene Blue From Aqueous Solution by Activated Carbon Embedded Zero-Valent Iron: Effect of Reduction Methods. Front. Environ. Sci. 9:799264. doi: 10.3389/fenvs.2021.799264

Zero valent iron (ZVI) particles were embedded into porous materials to avoid aggregation and separation problems in the controlled synthesis process. To investigate the adsorption mechanism of crystal violet and methylene blue, activated carbon (AC) and AC-based ZVI extraction by solid-phase and liquid-phase reduced approaches was conducted. Characterization methods of specific surface area, scanning electron microscopy (SEM), and x-ray diffractograms (XRD) were used to elucidate the structure of adsorbents, and the adsorption capacities of crystal violet and methylene blue were obtained under experimental conditions of various pH values (2.0–10.0), adsorption times (0–72 h), and temperatures (30–50°C). The adsorption of crystal violet/methylene blue was controlled by both chemisorption and reduction. The adsorption processes were fitted to a pseudo-second-order kinetic model, and that of reduction kinetics was suitable to pseudo-first-order kinetic model. The thermodynamic study revealed that the adsorption of crystal violet and methylene blue was endothermic and spontaneous, and the adsorption isotherms fitted well to the Langmuir model. Different adsorption capacities of crystal violet and methylene blue on various adsorbents were found, indicating that both the properties of adsorbents (pore size, specific surface area, and chemical functional groups) and the structures of adsorbates had significant effect on the removal of dye molecules.

Keywords: water pollution, activated carbon, zero valent iron, crystal violet, methylene blue

INTRODUCTION

Water pollution, a known universal crisis, might cause a reduction in the population, or extinction, of living things; reduce the value of environmental resources; and pose a threat to ecological balance (Iqbal et al., 2019; Efimov et al., 2019; Li et al., 2020). The release of dye in wastewater generated from different industries has been considered to be an important source of water pollution (Bilal et al., 2016a; Nouren et al., 2017). These dyes pose a serious threat to the ecological environment since they are extremely stable and non-biodegradable, and their accumulation always leads to poor oxygenation of the water environment by preventing the photosynthesis of photosynthetic

organisms (Spadaro et al., 1992; Xu et al., 2018). Moreover, most dyes are toxic, mutagenic, and carcinogenic, leading to serious harm for aquatic animals and human health (Bilal et al., 2016a; Bilal et al., 2016b; Ramamoorthy et al., 2020). Therefore, it is quite significant to carry out the remediation of dyes in wastewater to clean the water environment and safeguard human health (Abbas et al., 2018; Amin et al., 2020).

To impede the discharge and pollution of dye in wastewater, plenty of treatment methods have been continuously improved to remove these dyes from wastewater (Chen et al., 2017; Saber-Samandari et al., 2017). Considering economics, applicability, and removal efficacy, adsorption is suggested as the most popular technique (Fernandes et al., 2010; Xu et al., 2014; Rasalingam et al., 2015), in which the selection of adsorbents is the key factor affecting removal efficiency (Fernandes et al., 2010; Zhang et al., 2020b; Liu et al., 2014). Activated carbon (AC) is known as the most effective adsorbent; however, the expensive cost of AC restricts its wide utilization. Recently, a variety of bio-based activated carbons derived from agricultural wastes such as fruit peel, crop straw, coconut shell, and vegetable residues have been synthesized to make the adsorption process more feasible and cost-effective (Mishra et al., 2021). Moreover, iron-based porous materials have been developed to be effective adsorbents for toxic dye removal from wastewater (Zhang et al., 2010; Wang et al., 2012), mainly because of the unique redox potential of zero valent iron (ZVI) combined with the high surface area and large reaction sites of porous adsorbents (Kerkez et al., 2014). Previous studies demonstrated that iron-modified montmorillonite could effectively adsorb crystal violet (CV) (Guz et al., 2014), and iron nanoparticles decorated onto three-dimensional graphene could rapidly and efficiently degrade azo dye (Wang et al., 2015).

However, the application of ZVI in actual water treatment is subject to certain restrictions, because it tends to agglomerate and is easily oxidized (Liu et al., 2007; Fan et al., 2016). Therefore, many studies have been initiated to search for different matrices to overcome the iron particle aggregation, such as adding iron on montmorillonite for the adsorption of toxic cationic dyes (Wang et al., 2017; Liu et al., 2018) and adding iron nanoparticles onto three-dimensional graphene to degrade azo dyes (Liu et al., 2018). It could be found that two different approaches, namely, solid-phase and liquid-phase iron direct reduction technology (Liu et al., 2007; Wang et al., 2017; Liu et al., 2018), are the main approaches to prepare ZVI covered on adsorbents for effectively removing toxic dyes in wastewater. Using liquid-phase iron direct reduction technology, many materials were used as matrices to fix nZVI including kaolinite (Liu et al., 2007), activated carbon (Liu et al., 2018), graphene (Wang et al., 2017), and palygorskite (Ngulube et al., 2019), which exhibited an excellent dye removal efficiency. Based on solid-phase iron direct reduction technology, different kinds of iron-based adsorbents with the ZVI particles embedded into matrixes could be prepared, overcoming the lack of instability of ZVI synthesized in the liquid-phase direct reduction approach (Wang et al., 2017; Zheng et al., 2019).

In order to research the removal efficiency and purification mechanism of dyes onto AC embedded with ZVI extracted by solid/liquid-phase direct reduction approach, a series of AC supported ZVI adsorbents were synthesized and used to remove CV and methylene blue (MB) at various pH values, adsorption times, and temperatures. CV and MB were chosen as the representation of dyes because of the wide area of applications and similar molecular weights/different molecular structures. In this study, palm kernel shells as agricultural wastes were used to prepare AC adsorbents owing to their low ash content, high in carbon and volatile content (Ajeng et al., 2021). The higher heating value of palm kernel shells was beneficial for the solid-phase iron direct reduction technology (Wang et al., 2017; Bazargan et al., 2018). Thus, AC adsorbents were used as reductants to prepare the ZVI in the solid-phase iron direct reduction process and as matrices to fix nZVI in the liquid-phase iron direct reduction process. Adsorption data were interpreted by using adsorption kinetics, adsorption isotherms, and thermodynamic models to calculate the adsorption capacities and thermodynamic parameters.

MATERIALS AND METHODS

Materials and Chemicals

Palm kernel shell (C 50.2%, H 6.2%, O 40.8%, and N 0.3%), and iron ore tailings (Fe_2O_3 27.47%, Al_2O_3 6.44%, SiO_2 22.44%, CaO 1.95%, MgO 3.07%, and S_2O_3 4.61%) were sieved through 500-mesh screens and dried in an oven at 80°C for 24 h. Analytical grade dye molecules (CV and MB), iron chloride ($FeCl_3{\cdot}6H_2O$), ethanol, sodium borohydride ($NaBH_4$), and sodium hydroxide (NaOH) were purchased from Beijing Chemical Reagents Company (Beijing, China). Water used in this experiment was deionized water.

Preparation of Adsorbents

AC from palm kernel shell (PAC, 1#) and ZVI adsorbents produced through the solid-phase direct reduction approach (PAC-mZVI, 2#) were prepared as shown in **Figure 1**. In the preparation of PAC, palm kernel shell was heated in the absence of oxygen at a heating rate of 10°C min^{-1}, a heating temperature of 800°C, and a calcining time of 40 min, to maintain its weight and produce a loose porous structure. Schematic of the preparation steps is shown in **Figure 1**.

The solid-phase direct reduction approach was chosen to produce ZVI to prepare PAC-mZVI (2#), in which iron ore tailings were reduced by palm kernel shell to ZVI during the sintering process at high temperature, as shown in the chemical reaction below:

$$C + Fe_xO_y \rightarrow Fe_xO_{y-1} + CO\uparrow$$
$$CO + Fe_xO_y \rightarrow Fe_xO_{y-1} + CO_2\uparrow$$
$$H_2 + Fe_xO_y \rightarrow Fe_xO_{y-1} + H_2O$$

According to a previous study (Wang et al., 2017), the liquid-phase direct reduction approach was chosen to produce nanoscale ZVI to prepare PAC-nZVI (3#) adsorbents, in

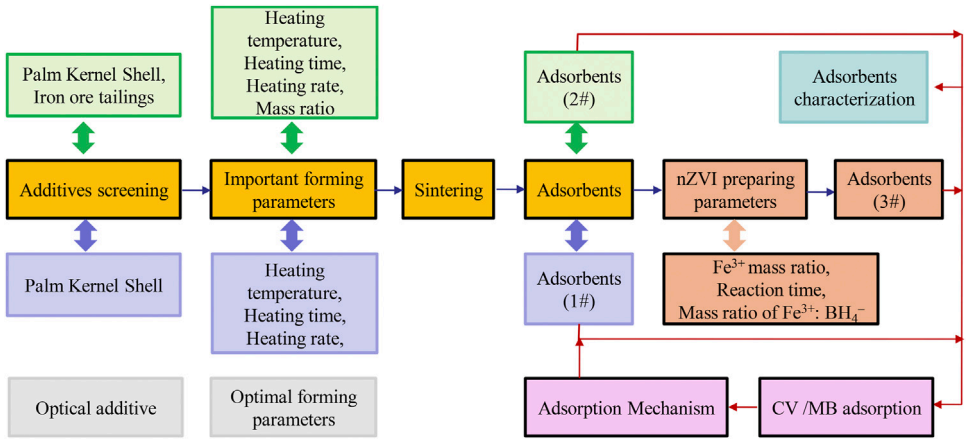

FIGURE 1 | Schematic of the preparation of the adsorbents.

which Fe^{3+} was reduced by $NaBH_4$ to ZVI on the surface of PAC as shown in the chemical reaction below:

$$2FeCl_3 + 6NaBH_4 + 18H_2O \rightarrow 2Fe^0 + 6NaCl + 6B(OH)_3 + 21H_2\uparrow$$

Iron chloride solution ($FeCl_3$) saturated PAC adsorbents and sodium borohydride solution ($NaBH_4$) were shaken at 120 r min^{-1} under a temperature of 30°C to reduce Fe^{3+} to ZVI. The optimal experimental factors influencing the amount of ZVI covered on the surface of PAC were selected at a shaking time of 1 h, a molar ratio of Fe^{3+}:BH_4^-at 1:3, and a mass ratio of Fe^{3+}:PAC adsorbent at 1:5.

Characterization

The surface area and pore size were detected according to nitrogen adsorption–desorption isotherms using the Autsorb-1 (Quantachrome, United States). The morphological characteristics and chemical components of these adsorbents were determined using scanning electron microscopy (SEM, JSM-6610 LV, Jeol, Japan) and x-ray diffractograms (XRD, 08 Advance Davinci, Bruker, Germany), respectively. Zeta potentials were determined by a Zeta Probe apparatus (Colloidal-Dynamics, United States).

Adsorption Experiments

Dye solution (100 ml) with an initial concentration of 50–1,000 mg L^{-1} and an adsorbent dose of 0.6 g were added into glass conical flasks to carry out the adsorption experiments at the constant speed of 120 rpm. The desired pH value was adjusted at the range of 2–10. Adsorption kinetic studies were carried out at various adsorption times (0–72 h). The removal efficiencies (R) and adsorption capacities (Q_t) were calculated by **Eqs 1**, **2** (Mwamulima et al., 2018). Adsorption isotherm studies were conducted with different initial concentrations of dye solution (50, 100, 200, 400, 600, 800, and 1,000 mg L^{-1}) at temperatures of 30, 40, and 50°C. The concentrations of residual CV and MB in aqueous solution were detected by UV spectrophotometry.

TABLE 1 | Textural features of palm kernel shell, PAC, PAC-mZVI, and PAC-nZVI adsorbents.

Sample	Palm kernel shell	PAC	PAC-mZVI	PAC-nZVI
S_{BET} (m^2/g)	125.12	1,075.23	445.39	725.94
S_{Micro} (m^2/g)	70.22	899.82	221.33	382.28
R_p (Å)	1,512.72	990.45	810.25	928.22

$$R = \frac{C_0 - C_t}{C_0} \times 100\% \quad (1)$$

$$Q_t = \frac{(C_0 - C_t)V}{m} \quad (2)$$

where C_0 (mg L^{-1}) is the initial concentration, C_t (mg L^{-1}) is the concentration at time t, V (L) is the volume of the solution, and m (g) is the adsorbent weight.

RESULTS AND DISCUSSION

Adsorbents Characterization

Nitrogen adsorption method was used to determine the pore diameter, pore volume, and surface area of adsorbents in **Table 1**. Compared with palm kernel shell, PAC, PAC-mZVI, and PAC-nZVI had a much larger surface area and micropore area, which might lead to the deduction that abundant micropores were generated in the process of biomass pyrolysis chemical reaction of palm kernel shell at high temperature (Guo et al., 2016). Moreover, the calcining temperature in the preparation of PAC-mZVI adsorbents had a significant impact on the reduction process, which largely determined the micropore area and pore size. The surface area of PAC-nZVI adsorbents was higher than the other three adsorbents, showing that the adsorbents prepared by the liquid-phase reduction approach had the largest BET surface area.

SEM and EDX images of PAC, PAC-mZVI, and PAC-nZVI are shown in **Figure 2**. It could be clearly found that the

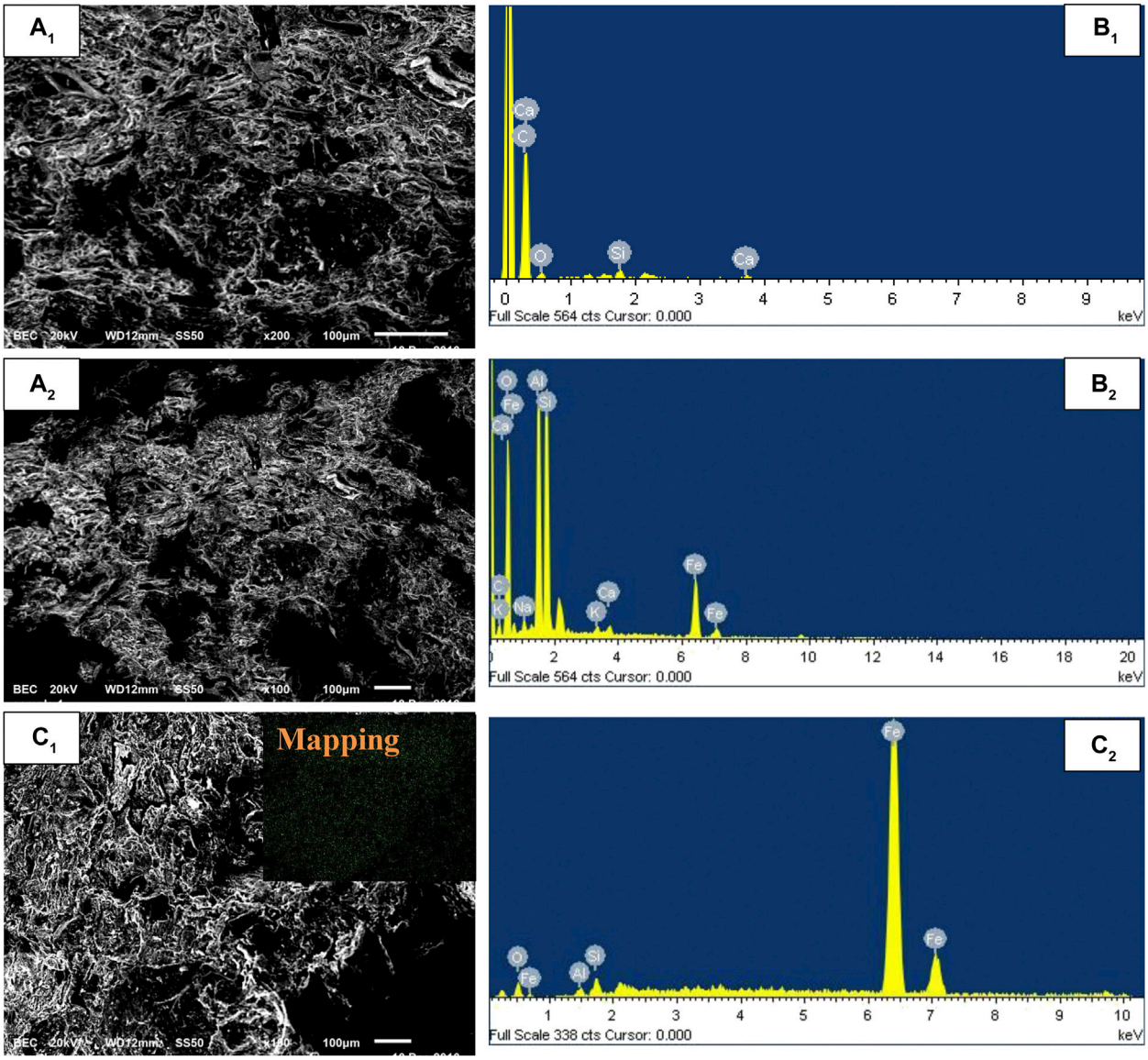

FIGURE 2 | SEM images of **(A_1)** PAC, **(B_1)** PAC-mZVI, and **(C_1)** PAC-nZVI and EDX images of **(A_2)** PAC, **(B_2)** PAC-mZVI, and **(C_2)** PAC-nZVI.

surface of these adsorbents was rough; meanwhile, numerous pores existed in these adsorbents. This could be attributed to the fact that the organic matter in palm kernel shell generated volatile CO, CO_2, and hydrogen during the sintering process (Guo et al., 2016). These volatile gases escaped from the inside of adsorbents; then, the pores were formed in this process. Moreover, PAC-nZVI adsorbents contained more pores compared with PAC-mZVI adsorbents, which might be attributed to the cementation effect of ZVI particle in the solid-phase reduction process (Wang et al., 2017). Combined with EDX analysis, it could be found that ZVI was generated in the solid-phase reduction reaction with the reductants of palm kernel shell and liquid-phase reduction reaction process in aqueous solution. As shown in **Figure 2C**, newly formed ZVI particles in the liquid-phase reduction reaction process were uniformly dispersed throughout the matrix, owing to the advantages of the liquid-phase iron reduction approach.

XRD analyses were chosen to identify various phases and phase transformations for PAC, PAC-mZVI, and PAC-nZVI adsorbents. As depicted in **Figure 3A**, the main component of PAC adsorbents was carbon. As for PAC-mZVI in **Figure 3B**, hematite (Fe_2O_3) and ZVI were found as well as the carbon that PAC contained, indicating that palm kernel shells were translated to PAC, and iron ore tailings were partly reduced to ZVI in the solid reduction process with palm kernel shell as reductants (Man et al., 2014; Wang et al., 2017). As shown in **Figure 3C**, PAC-nZVI adsorbents mainly contained carbon and ZVI. Compared with PAC-mZVI adsorbents, ZVI was the unique form of iron element in PFB-nZVI adsorbents, confirming that Fe^{3+} was directly reduced to ZVI covered on porous adsorbents in

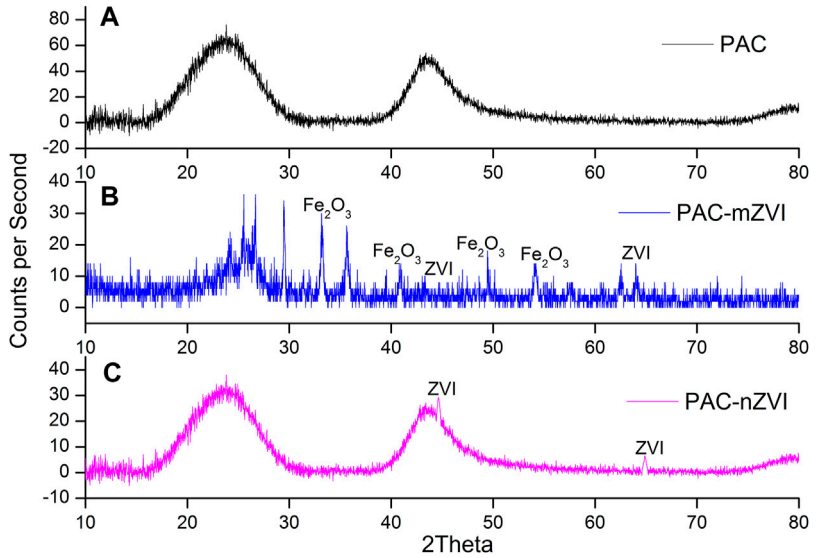

FIGURE 3 | X-ray diffractograms of three different adsorbents. **(A)** PAC, **(B)** PAC-mZVI, and **(C)** PAC-nZVI.

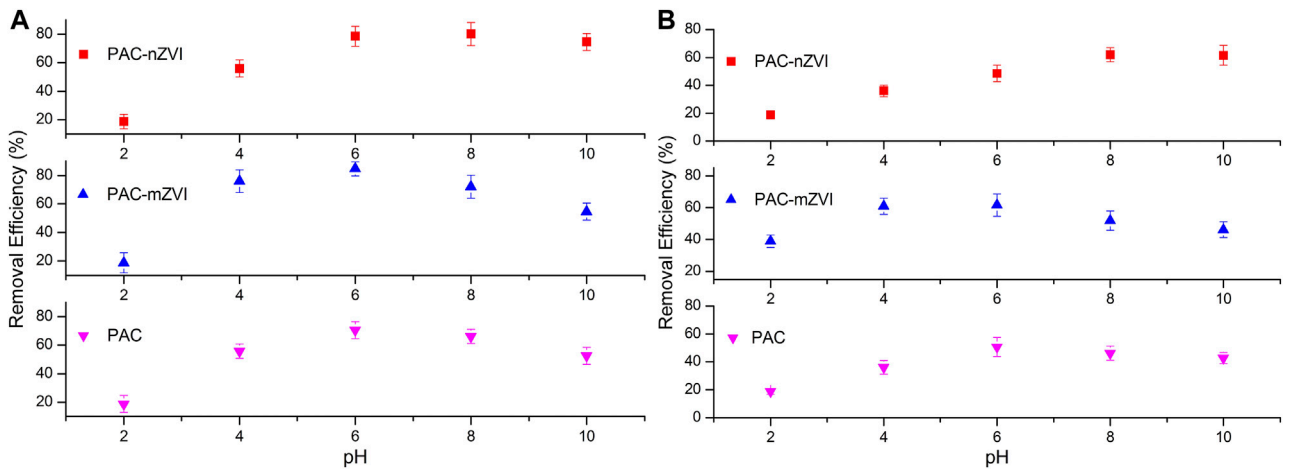

FIGURE 4 | Effects of pH on the removal of CV **(A)** and MB **(B)** by PAC, PAC-mZVI, and PAC-nZVI adsorbents.

liquid-phase reduction approach (Liu et al., 2018; Mwamulima et al., 2018).

Effects of pH on Crystal Violet and Methylene Blue Removal

Removal efficiencies of CV and MB by PAC, PAC-mZVI, and PAC-nZVI adsorbents were researched at different pH values, and effects of pH value on adsorption capacity are shown in **Figure 4**. The adsorption process was significantly affected by the changing of pH value, mainly because the existence forms of functional groups on the adsorbents were changed under different acid and alkali conditions (Wang et al., 2017; Liu et al., 2018; Mwamulima et al., 2018). As shown in **Figure 4**, removal efficiencies of dye molecules increased with the increase of pH value at the initial stage, then gradually decreased after the maximum. Meanwhile, we could find that removal efficiencies of CV by these three different adsorbents reached the maximum when pH value was approximately at 6.0, 6.0 and 8.0, respectively.

This phenomenon could be attributed to the influence of structure characteristics and the point of zero charge (pH_{pzc}) of adsorbents. As reported in previous literature, the surface of adsorbent had a positive charge at pH < pH_{pzc}, negative charge at pH > pH_{pzc}, and net zero charge at pH = pH_{pzc}, respectively (Hammed et al., 2016). In this study, pH_{pzc} of PAC, PAC-mZVI, and PAC-nZVI adsorbents was approximately 5.5, 7.0, and 8.0, respectively. At lower pH, excess H^+ might compete with CV/MB molecule for adsorption sites, inhibiting the adsorption process of

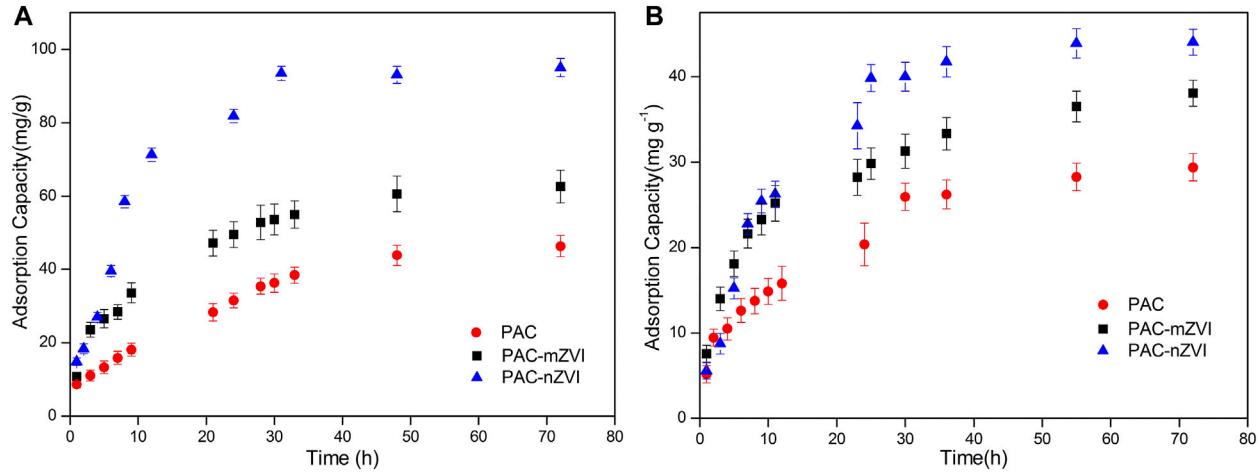

FIGURE 5 | Effects of contact time on the removal of CV **(A)** and MB **(B)** by PAC, PAC-mZVI, and PAC-nZVI adsorbents.

CV and MB onto adsorbents. Moreover, electrostatic repulsion existed between adsorbents and dye molecules, which would be also largely adverse to the adsorption of CV/MB onto adsorbents. Generally, cationic dyes were quite easily absorbed onto adsorbents with negative charges owing to the attraction of positive and negative charges. It could be concluded that excess OH^- at higher pH promoted the formation of iron hydroxide, which could occupy the reactive sites on adsorbents to decrease the reduction reaction of CV/MB in this experiment (Chen et al., 2013).

Effects of Contact Time on Crystal Violet and Methylene Blue Removal

The adsorption capacities of CV and MB at 30°C are shown in **Figure 5**. The adsorption processes of CV/MB were generally fast at the initial stage and then leveled off with time, which was attributed to the fact that huge amounts of active vacant sites on these adsorbents were gradually occupied. As depicted in **Figures 5A,B**, the adsorption of CV and MB on PAC-nZVI reached equilibrium at approximately 50 h, which was slightly longer than other adsorbents. The reason was that the specific surface area of PAC-nZVI adsorbents was larger than that of other adsorbents and a large number of pores existed in the interior of the adsorbents. Moreover, the adsorption capacity of PAC-nZVI adsorbents for CV and MB arrived at 97 mg g^{-1} and 43 mg g^{-1}, which was higher than that of other adsorbents. This could be attributed to the fact that both adsorption and reduction reactions were included in the removal processes of CV and MB by these three different adsorbents. PAC-nZVI adsorbents contained higher concentration of ZVI compared with that of other adsorbents, generating more active sites to promote the increase in adsorption capacity. Besides, it could be found that the absorption of MB reached the equilibrium faster than that of CV, which could be attributed to the fact that the triangular shape of CV was not beneficial when entering smaller pores compared with the chain shape of MB.

Effects of Temperature on Crystal Violet and Methylene Blue Removal

Changes in adsorption capacity of CV and MB under different temperatures are depicted in **Figure 6**. It could be found that the adsorption capacity of CV/MB increased with the increase of temperature, indicating that the adsorption processes of dye molecules were endothermic reaction. Moreover, the phenomenon could also be explained by the fact that high temperature could promote the increase in pore size and surface area to enlarge the adsorption capacity (Liu et al., 2018). When the temperature arrived at 50°C, the adsorption capacity of PAC-nZVI for CV and MB arrived at approximately 110 and 73 mg g^{-1}, respectively. Moreover, the change rate of adsorption capacity with time increased as the reaction temperature increased. It might be attributed to the increase in the mobility of dye molecules in aqueous solution and the formation of reactive sites on the interface of adsorbents under higher temperature (Liu et al., 2018; Mwamulima et al., 2018).

Kinetic Study

Adsorption Kinetics

Lagergren pseudo-first-order rate (**Eq. 3**) (Lagergren, 1898), pseudo-second-order rate (**Eq. 4**) (Ho and McKay, 1999), and Weber-Morris diffusion model (**Eq. 5**) (Weber and Morris, 1963) were chosen to explain the kinetics of CV and MB onto these three adsorbents, which could be described as:

$$\log(q_e - q_t) = \log q_e - \frac{k_1}{2.303}t \quad (3)$$

$$\frac{t}{q_t} = \frac{1}{k_2 q_e^2} + \frac{1}{q_e}t \quad (4)$$

$$q_t = k_{\text{int}} t^{0.5} + b \quad (5)$$

where q_e (mg g^{-1}) and qt (mg g^{-1}) are the adsorption capacities at equilibrium and time t, respectively. k_1 (1/h), k_2 (1/h), k_{int}, and b are the constants in pseudo-first-order, pseudo-second-order, and intraparticle diffusion, respectively.

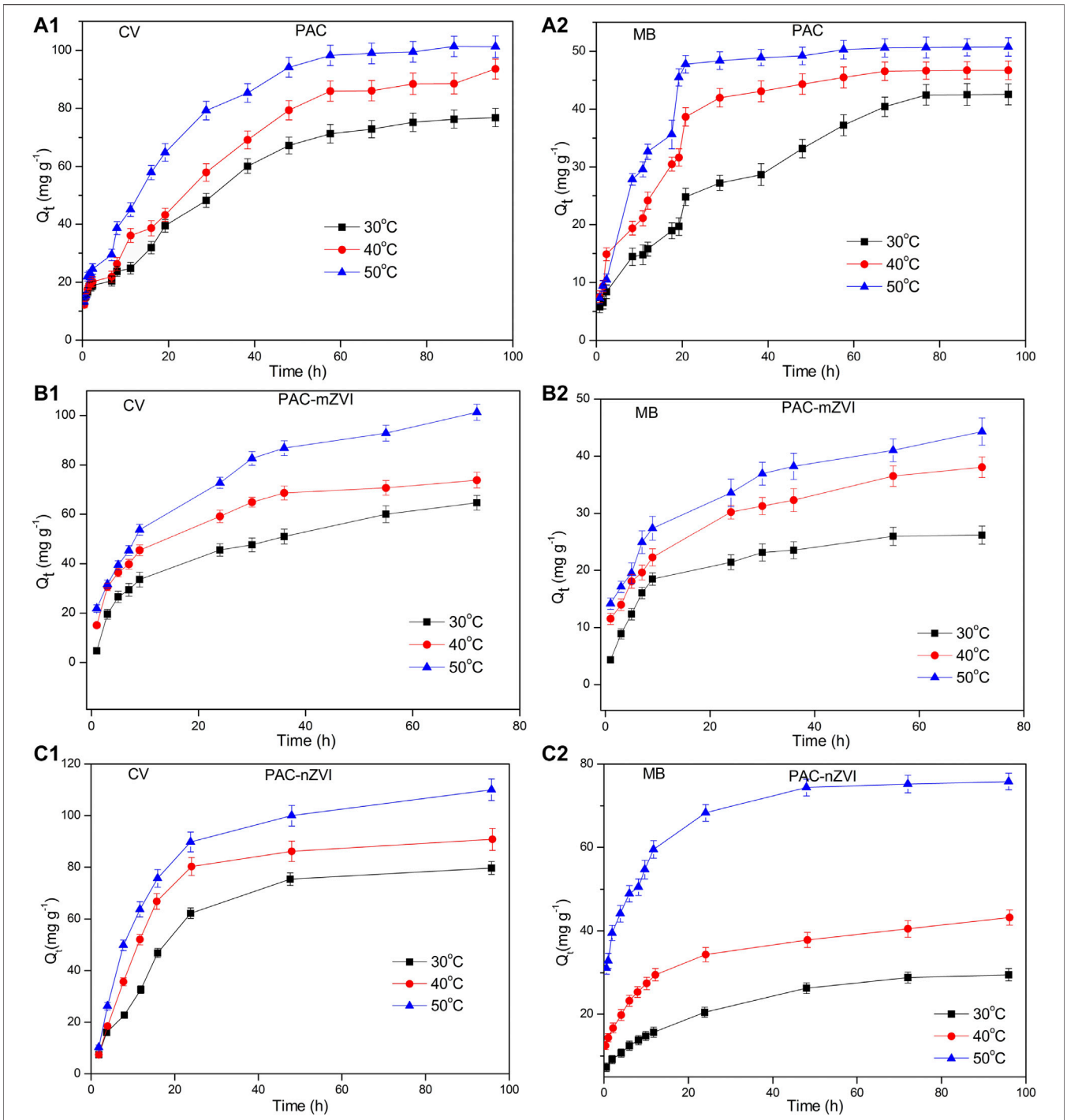

FIGURE 6 | Effects of temperature on the removal of CV and MB by PAC, PAC-mZVI, and PAC-nZVI adsorbents.

The kinetic parameters (r^2, Q_e, K_1, and K_2 values) are shown in **Table 2**. According to the previous literature, the optimal fitting model could be selected based on the parameter of r^2 value (Wang et al., 2017). Thus, it could be found that adsorption of CV/MB onto these three adsorbents fitted the pseudo-second-order rate equations well due to the relatively better r^2 values compared with that of the pseudo-first-order kinetic model. Based on the q_e values calculated from the pseudo-second-order kinetics model, PAC-nZVI adsorbent showed the highest adsorption capacities at equilibrium compared with other adsorbents. These values of q_e had quite good agreement with experimental results. Thus, we could deduce that chemisorption was the rate-controlling step in the removal process of CV/MB onto PAC and PAC-based ZVI adsorbents (Liu et al., 2018; Mwamulima et al., 2018).

TABLE 2 | Kinetic parameters for the adsorption of CV and MB dye on PAC and PAC-based ZVI adsorbents.

Adsorbents	T	Pseudo-first-order kinetic model						Pseudo-second-order kinetic equation					
		CV			MB			CV			MB		
		r^2	q_e	K_1	r^2	Q_e	K_1	r^2	q_e	K_2	r^2	q_e	K_2
PAC	30	0.9779	66	0.012	0.9536	48	0.0244	0.9862	76	0.00014	0.9666	54	0.0003
	40	0.9701	84	0.015	0.9740	53	0.0244	0.9633	91	8.1e-5	0.9770	54	0.0003
	50	0.9703	87	0.013	0.9110	66	0.025	0.9869	95	7.57e-5	0.9734	60	0.0002
	30	0.9446	58	0.104	0.8973	25	0.151	0.9963	69	0.0018	0.9919	31	0.0043
PAC-mZVI	40	0.9299	66	0.160	0.9108	33	0.142	0.9936	76	0.0025	0.9939	41	0.0036
	50	0.8687	75	0.113	0.8955	35	0.142	0.9906	100	0.0014	0.9934	53	0.0035
	30	0.8324	63	0.0035	0.9546	27	0.0005	0.9963	72	0.0039	0.9924	32	0.0022
PAC-nZVI	40	0.8531	79	0.0058	0.9668	38	0.0005	0.9926	84	0.0095	0.9652	42	0.0015
	50	0.8176	92	0.0051	0.9689	63	0.0010	0.9982	102	0.0183	0.9948	69	0.0044

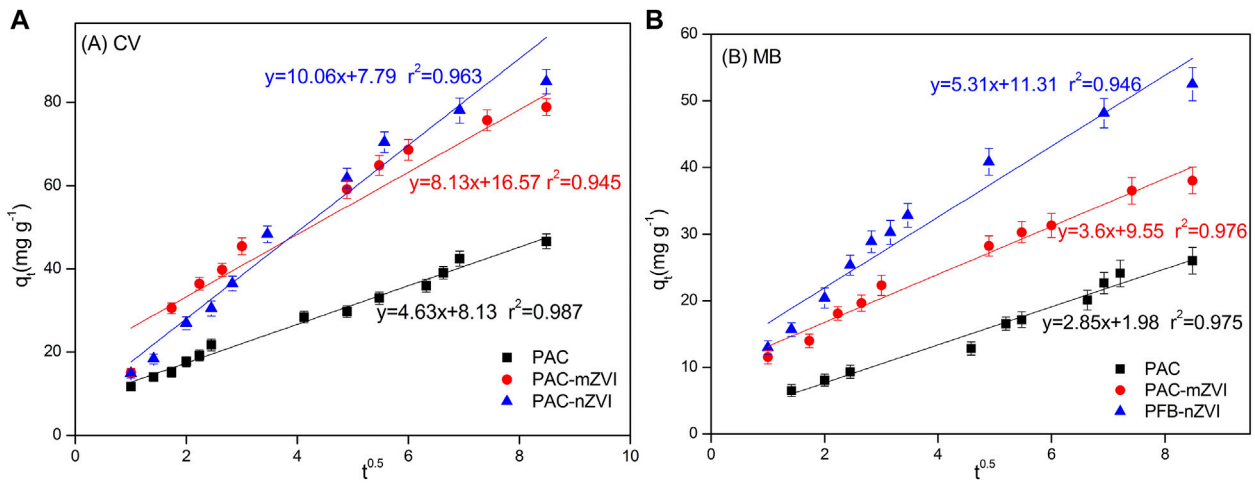

FIGURE 7 | Intraparticle model for the adsorption for the adsorption of CV and MB onto PAC, PAC-mZVI, and PAC-nZVI adsorbents.

TABLE 3 | Reduction kinetic parameters of CV and MB dyes on PAC and PAC-based ZVI adsorbents.

Adsorbents	T	Pseudo-first-order kinetic model				Pseudo-second-order kinetic equation			
		CV		MB		CV		MB	
		r^2	K_{obs}	r^2	K_{obs}	r^2	K	r^2	K
PAC	30	0.9569	0.003	0.9512	0.0001	0.9121	0.0093	0.9452	0.0002
	40	0.9715	0.0055	0.9621	0.0002	0.9352	0.0135	0.9522	0.0003
	50	0.9828	0.0063	0.9788	0.0008	0.9352	0.0135	0.9624	0.0006
	30	0.9919	0.0716	0.9967	0.0164	0.9638	0.00041	0.9968	0.00005
PAC-mZVI	40	0.9914	0.0756	0.9961	0.0348	0.8834	0.00042	0.9760	0.00012
	50	0.9918	0.0827	0.9932	0.0627	0.8835	0.0005	0.9485	0.00022
	30	0.9853	0.0029	0.9575	6e-5	0.9539	0.0060	0.8721	0.0004
PAC-nZVI	40	0.9520	0.0040	0.9608	8e-5	0.7635	0.0060	0.8093	0.0005
	50	0.8454	0.0042	0.9243	0.0002	0.6879	0.0060	0.8540	0.0005

In order to further analyze the adsorption process, the Weber-Morris diffusion model was chosen to discuss the relationship between q_t and $t^{0.5}$ based on the intraparticle diffusion theory. If the intraparticle diffusion was a rate-limiting step, the plot of q_t against $t^{0.5}$ would yield a straight line with a slope of k_{int}. As depicted in **Figures 7A, B**, the linear plot of q_t vs. $t^{0.5}$ yielded a straight line, indicating that intraparticle diffusion was a rate-limiting step. Moreover, the linear plot did not pass

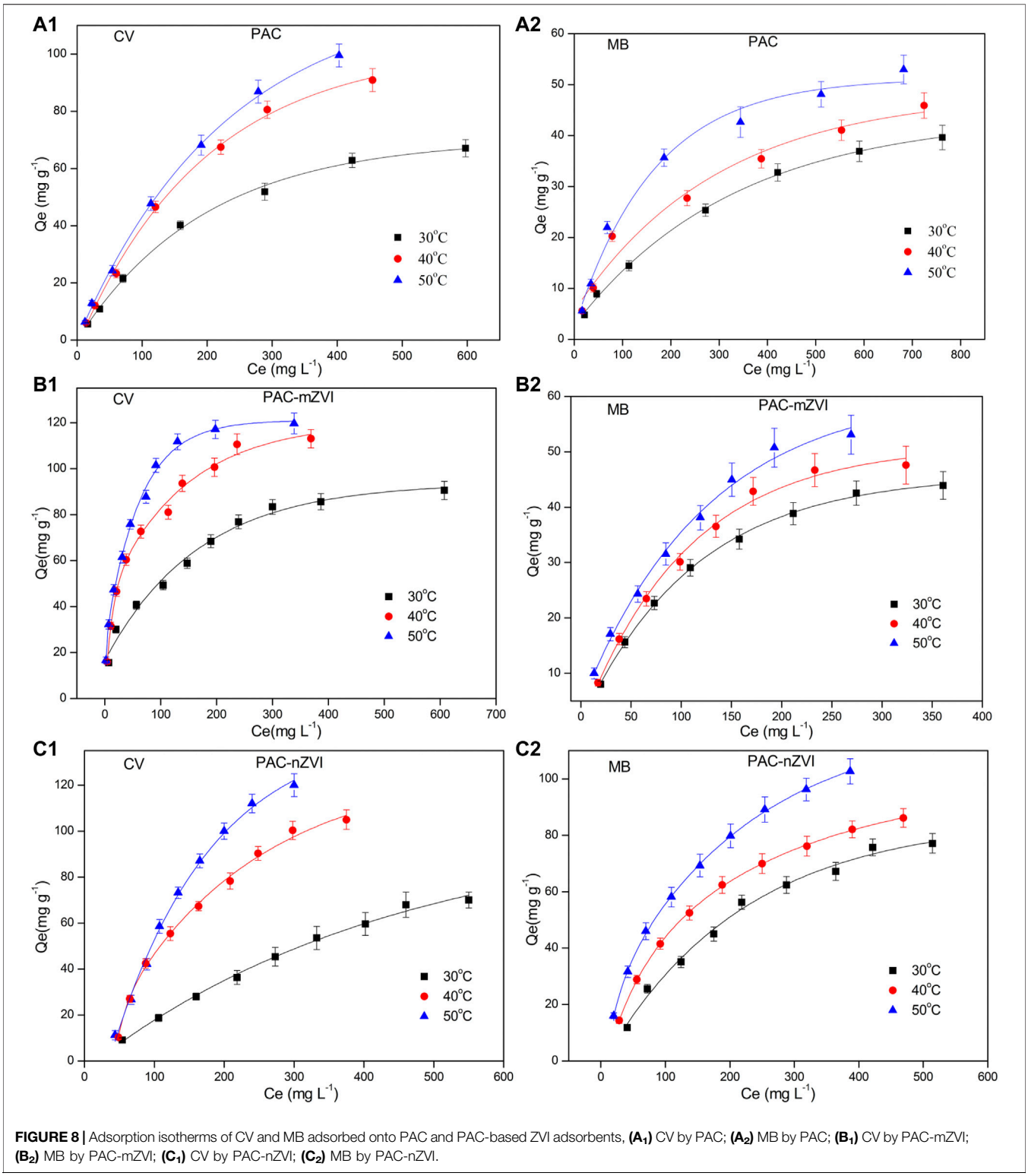

FIGURE 8 | Adsorption isotherms of CV and MB adsorbed onto PAC and PAC-based ZVI adsorbents, **(A_1)** CV by PAC; **(A_2)** MB by PAC; **(B_1)** CV by PAC-mZVI; **(B_2)** MB by PAC-mZVI; **(C_1)** CV by PAC-nZVI; **(C_2)** MB by PAC-nZVI.

through the origin, illustrating that the molecular diffusion controlled the adsorption reaction rate to some extent. Thus, it could be concluded that two processes, namely, chemisorption and diffusion, affected the removal process of these dye molecules.

Reduction Kinetics

Based on the above research results, adsorption reaction of CV/MB by PAC and PAC-based ZVI adsorbents included adsorption and chemical reduction (Chen et al., 2013; Wang et al., 2017; Ezzatahmadi et al., 2017). Pseudo-first-order and -second-order

TABLE 4 | Parameters for the adsorption isotherms of CV and MB on PAC and PAC-based ZVI adsorbents.

Adsorbents	T	Langmuir						Freundlich					
		CV			MB			CV			MB		
		r^2	q_m	b	r^2	q_m	b	r^2	K_f	1/n	r^2	K_f	1/n
PAC	30	0.9684	98	0.015	0.9968	60	0.0083	0.9862	7.6	0.414	0.9633	1.6	0.587
	40	0.9872	120	0.027	0.9879	68	0.0085	0.9633	10.1	0.451	0.9678	1.7	0.612
	50	0.9879	132	0.037	0.9823	74	0.0099	0.9869	13.2	0.439	0.9908	2.4	0.576
	30	0.9992	110	0.002	0.9935	38	0.0038	0.9632	2.2	0.545	0.9959	1.0	0.554
PAC-mZVI	40	0.9991	159	0.0023	0.9906	67	0.0045	0.9402	2.8	0.584	0.9797	2.2	0.463
	50	0.9961	204	0.0027	0.9968	84	0.0051	0.9715	1.7	0.672	0.9571	2.9	0.450
	30	0.9772	95	0.017	0.7728	68	0.0012	0.9456	2.8	0.710	0.9946	0.7	0.767
PAC-nZVI	40	0.9325	163	0.012	0.8732	79	0.0043	0.8840	21.3	0.221	0.9255	1.8	0.683
	50	0.9947	344	0.086	0.6039	99	0.0005	0.8568	55.1	0.382	0.9956	0.5	0.938

TABLE 5 | Thermodynamic parameters for the adsorption of CV and MB on PAC and PAC-based ZVI adsorbents.

Adsorbents	Temp	CV			MB		
		ΔG	ΔH	ΔS	ΔG	ΔH	ΔS
PAC	30	−4.49	38.01	140.65	−2.45	29.30	60.65
	40	−6.25			−2.61		
	50	−7.29			−3.10		
PAC-mZVI	30	−16.89	12.21	95.98	−17.89	12.12	99.08
	40	−17.81			−18.92		
	50	−18.81			−19.86		
PAC-nZVI	30	−22.06	80.40	334.05	−14.99	100.76	382.01
	40	−23.02			−18.81		
	50	−24.04			−22.78		

reduction kinetic models in **Eqs 6**, **7** were selected to study the reduction process (Kerkez et al., 2014).

$$\ln \frac{C_t}{C_0} = -k_{obs}t \tag{6}$$

$$\ln\left(\frac{1}{C_t} - \frac{1}{C_0}\right) = k_2 t \tag{7}$$

where C_0 (mg g^{-1}) and C_t (mg g^{-1}) are the concentration at the initial time and at time t; k_{obs} (h^{-1}) and k_2 (h^{-1}) are the rate constant of pseudo-first-order and second-order reaction, respectively.

Reduction kinetics parameters are shown in **Table 3**. Based on the reduction kinetics parameters, the pseudo-first-order kinetics model provided a better match of the experiment results of CV/MB dye, because of the relatively better r^2 values compared with that of the pseudo-second-order kinetic model. This indicated that CV/MB reacted with ZVI in the interface of the adsorbents through a solid–liquid reaction (Wang et al., 2017; Liu et al., 2018). Moreover, the reduction processes of CV/MB by these three adsorbents were endothermic, considering the reduction kinetic rate (k_{obs}) increased with the increase of temperature from 30 to 50°C. This was due to the fact that higher temperature could promote dye molecule transfer from aqueous solution to the surface of adsorbents (Adesemuyi et al., 2020).

Taking PAC-mZVI adsorbent for example, k_{obs} increased from 0.0716 to 0.0827 h^{-1} when the temperature increased from 30 to 50°C. It was depicted that the K_{obs} value of PAC-mZVI adsorbents was slightly higher, indicating that the chemical reduction reaction happened faster than that of the other two adsorbents. Based on the parameter values shown in **Tables 2**, **3**, it could be deduced that both physical adsorption and chemical reaction might handle the removal processes of CV/MB onto these adsorbents. Meanwhile, we could also find that the adsorption process of CV/MB dye was slightly faster than the reduction process by the comparison of the parameters of K_1 and K_{obs} (Chen et al., 2013).

Adsorption Isotherms

Adsorption isotherms could reveal the relationship of adsorption capacity of adsorbents and the concentration of adsorbates in aqueous solution, when the adsorption process reached equilibrium at a certain temperature. In this study, the Langmuir equation in **Eq. 8** (Langmuir, 1918) and the Freundlich equation in **Eq. 9** (Freundlich, 1906) were chosen to study the adsorption isotherms. The Langmuir equation supposed that adsorption was limited to monolayer coverage, while Freundlich isotherms assumed that the adsorption surface was heterogeneous and multilayer adsorption might be possible.

$$\frac{1}{q_e} = \frac{1}{q_{\max}C_e} + \frac{1}{q_{\max}} \tag{8}$$

$$\log q_e = \log K_F + \frac{1}{n}\log C_e \tag{9}$$

where C_e (mg L^{-1}) is the concentration of adsorbates at equilibrium, $q_{\max}$ (mg g^{-1}) is the maximum adsorption capacity, and K_F and n are constants related to adsorption capacity and intensity, respectively. Based on **Eqs 8**, **9**, it could be found that the near-perfect linear fitting of $1/q_e$ vs. $1/C_e$ belonged to the Langmuir model, while that of $\log q_e$ versus $\log C_e$ obeyed the Freundlich model. If the value of $1/n$ was less than 1, it might be attributed to the favorability of adsorption (Inbaraj and Chen., 2011; Fan et al., 2017).

The adsorption isotherms are depicted in **Figure 8**, and relevant adsorption isotherm parameters (b, Q_m, $1/n$, K_f) are shown in **Table 4**. Considering the relatively better r^2 values, we could find that adsorption isotherms of CV/MB matched well with the Langmuir model. Consequently, adsorption processes of CV/MB onto PAC and PAC-based ZVI adsorbents were homogeneous and

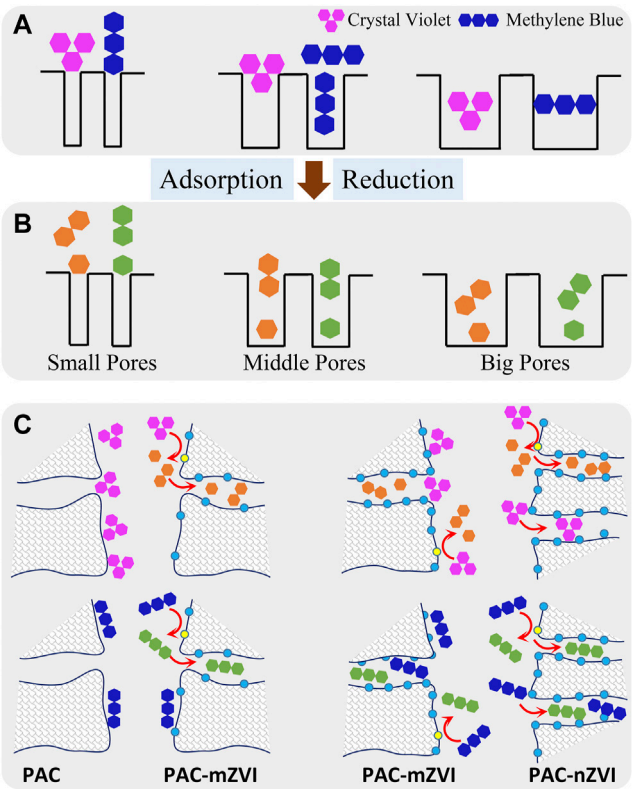

FIGURE 9 | A model of dye molecule (CV, MB) removal process by PAC and PAC-based ZVI adsorbents.

occurred at a monolayer region on the adsorbents. For the adsorption of CV dye, the Q_m value of PAC-nZVI adsorbents was the greatest compared with other adsorbents. As for MB, the Q_m value of PAC-nZVI adsorbents was 68, 79, and 99 mg g^{-1} at 30, 40, and 50°C, depicting the greatest adsorption capacity. Moreover, R_L values of CV and MB were less than 1, confirming that it was favorable for CV and MB adsorbed onto these adsorbents under this reaction condition (Inbaraj and Chen., 2011).

Thermodynamic Study

To analyze the effects of temperature on the adsorption, thermodynamic parameters including ΔH, ΔS, and ΔG were calculated based on the adsorption isotherms. The specific calculation method is shown as **Eqs 10**, **11**, respectively.

$$\Delta G = -RT \ln K \tag{10}$$

$$\ln K = \frac{\Delta S}{R} - \frac{\Delta H}{RT} \tag{11}$$

The parameter values of ΔH, ΔS, and ΔG are shown in **Table 5**. As noted, ΔG values of three different adsorbents decreased with the increase in temperature, indicating that the adsorption of CV/MB happened spontaneously. Meanwhile, ΔH values were all greater than zero, attributing to the fact that CV/MB adsorbed on adsorbents showed endothermic reactions. Moreover, values of ΔS in the adsorption processes were positive, which could further reveal the increasing randomness at the interface of solid/solution (Zhang et al., 2020a).

Mechanisms of Crystal Violet and Methylene Blue Removal by Adsorbents

CV and MB in water solution were firstly adsorbed on the surface of adsorbents, and then transported into the interior pores of adsorbents through pore diffusion. During the diffusion process, both the structural features of adsorbents and adsorbates had significant effects on the adsorption of dye molecules. When the molecular size of adsorbents was smaller than pore size, adsorbates could enter the internal pores for further adsorption action. Since the molecular structures of MB (line-shaped) and CV (fork-shaped) were different, the co-influence of the pore size of adsorbents and the structure of adsorbates on the removal processes is exhibited in **Figure 9A**.

CV and MB in the internal pores of adsorbents were finally adsorbed on the active sites of adsorbents, in which CV/MB was partly reduced by ZVI on the adsorbents. According to our previous research (Wang et al., 2017; Liu et al., 2018), CV was cleaved to two parts to generate new products *via* electrochemical reduction; however, MB reacted to its reduction state. The adsorption capacities of CV on these adsorbents were largely higher than that of MB as demonstrated in the experimental results, which might be attributed to the new products reduced from CV with smaller molecular size. Moreover, it could be deduced that specific surface area was also an important factor in the adsorption processes. The adsorption sites on the adsorbents increased with the increase in specific surface area. Based on the above discussion, the possible removal mechanisms of CV/MB from aqueous solutions on PAC and PAC-based ZVI adsorbents are proposed in **Figure 9**.

CONCLUSION

Adsorption of CV/MB on PAC and PAC-based ZVI adsorbents indicated that ZVI could efficiently remove cationic dyes from aqueous solution. The removal processes of CV/MB on adsorbents were significantly affected by the changing pH value, reaction time, and temperature. The adsorption capacities of CV/MB were fast in the initial stages and finally leveled off with time. The adsorption capacity increased with the increase in temperature. The adsorption processes of CV and MB onto these adsorbents all fitted well with the pseudo-second-order rate equations, and chemisorption was the rate-controlling step. The pseudo-first-order reduction kinetic model provided a better match of the adsorption process, indicating that dye molecules reacted with ZVI in the interface of adsorbents through a solid–liquid reaction, and the reduction process was endothermic. The adsorption isotherms obeyed the Langmuir model, indicating that CV/MB onto these adsorbents were homogeneous and occurred within a monolayer region on the surface of adsorbents. Compared with solid-phase iron direct reduction technology, PAC-nZVI adsorbents prepared by liquid-phase iron direct reduction technology showed higher adsorption capacity owing to the larger BET surface area and more ZVI particles. Furthermore, it was found that the properties of

adsorbents (pore size, specific surface area, and chemical functional groups) and the structure characteristics of adsorbates had significant effects on the adsorption efficiency of dye molecules.

DATA AVAILABILITY STATEMENT

The original contributions presented in the study are included in the article/supplementary material. Further inquiries can be directed to the corresponding author.

AUTHOR CONTRIBUTIONS

YW compiled and analyzed output data, and designed and wrote the first version of the manuscript. TC designed the study and managed the funding acquisition. XZ and TM conducted the experiments. All authors edited and approved the final version of this manuscript.

FUNDING

This study was financially supported by China Postdoctoral Science Foundation (grant number 2017M622301).

ACKNOWLEDGMENTS

The authors would like to thank Gang Zhou's team at Shandong University of Science and Technology who helped with the sampling and analysis.

REFERENCES

Abbas, M., Adil, M., Ehtisham-ul-Haque, S., Munir, B., Yameen, M., Ghaffar, A., et al. (2018). Vibrio Fischeri Bioluminescence Inhibition Assay for Ecotoxicity Assessment: A Review. *Sci. Total Environ.* 626, 1295–1309. doi:10.1016/j.scitotenv.2018.01.066

Adesemuyi, M. F., Adebayo, M. A., Akinola, A. O., Olasehinde, E. F., Adewole, K. A., and Lajide, L. (2020). Preparation and Characterisation of Biochars from Elephant Grass and Their Utilisation for Aqueous Nitrate Removal: Effect of Pyrolysis Temperature. *J. Environ. Chem. Eng.* 8, 104507. doi:10.1016/j.jece.2020.104507

Ajeng, A. A., Abdullah, R., Junia, A., Lau, B. F., Ling, T. C., and Ismail, S. (2021). Evaluation of palm Kernel Shell Biochar for the Adsorption of Bacillus Cereus. *Phys. Scr.* 96, 105004. doi:10.1088/1402-4896/ac0f3b

Amin, M., Chetpattananondh, P., and Khan, M. N. (2020). Ultrasound Assisted Adsorption of Reactive Dye-145 by Biochars from marine Chlorella Sp. Extracted Solid Waste Pyrolyzed at Various Temperatures. *J. Environ. Chem. Eng.* 8, 104403. doi:10.1016/j.jece.2020.104403

Bazargan, A., Rough, S. L., and McKay, G. (2018). Fine Tuning of Process Parameters for Improving Briquette Production from palm Kernel Shell Gasification Waste. *Environ. Tech.* 39, 931–938. doi:10.1080/09593330.2017.1317835

Bilal, M., Iqbal, M., Hu, H., and Zhang, X. (2016a). Mutagenicity and Cytotoxicity Assessment of Biodegraded Textile Effluent by Ca-Alginate Encapsulated Manganese Peroxidase. *Biochem. Eng. J.* 109, 153–161. doi:10.1016/j.bej.2016.01.020

Bilal, M., Iqbal, M., Hu, H., and Zhang, X. (2016b). Mutagenicity, Cytotoxicity and Phytotoxicity Evaluation of Biodegraded Textile Effluent by Fungal Ligninolytic Enzymes. *Water Sci. Technol.* 73, 2332–2344. doi:10.2166/wst.2016.082

Chen, J., Leng, J., Yang, X., Liao, L., Liu, L., and Xiao, A. (2017). Enhanced Performance of Magnetic Graphene Oxide-Immobilized Laccase and its Application for the Decolorization of Dyes. *Molecules* 22, 221. doi:10.3390/molecules22020221

Chen, Z., Wang, T., Jin, X., Chen, Z., Megharaj, M., and Naidu, R. (2013). Multifunctional Kaolinite-Supported Nanoscale Zero-Valent Iron Used for the Adsorption and Degradation of crystal Violet in Aqueous Solution. *J. Colloid Interf. Sci.* 398, 59–66. doi:10.1016/j.jcis.2013.02.020

Efimov, M. N., Vasilev, A. A., Muratov, D. G., Baranchikov, A. E., and Karpacheva, G. P. (2019). IR Radiation Assisted Preparation of KOH-Activated Polymer-Derived Carbon for Methylene Blue Adsorption. *J. Environ. Chem. Eng.* 7, 103514. doi:10.1016/j.jece.2019.103514

Ezzatahmadi, N., Ayoko, G. A., Millar, G. J., Speight, R., Yan, C., Li, J., et al. (2017). Clay-supported Nanoscale Zero-Valent Iron Composite Materials for the Remediation of Contaminated Aqueous Solutions: a Review. *Chem. Eng. J.* 312, 336–350. doi:10.1016/j.cej.2016.11.154

Fan, M., Li, T., Hu, J., Cao, R., Wu, Q., Wei, X., et al. (2016). Synthesis and Characterization of Reduced Graphene Oxide-Supported Nanoscale Zero-Valent Iron (nZVI/rGO) Composites Used for Pb(II) Removal. *Materials* 9, 687. doi:10.3390/ma9080687

Fan, S., Wang, Y., Wang, Z., Tang, J., Tang, J., and Li, X. (2017). Removal of Methylene Blue from Aqueous Solution by Sewage Sludge-Derived Biochar: Adsorption Kinetics, Equilibrium, Thermodynamics and Mechanism. *J. Environ. Chem. Eng.* 5, 601–611. doi:10.1016/j.jece.2016.12.019

Fernandes, A. N., Almeida, C. A. P., Debacher, N. A., and Sierra, M. M. D. S. (2010). Isotherm and Thermodynamic Data of Adsorption of Methylene Blue from Aqueous Solution onto Peat. *J. Mol. Struct.* 982, 62–65. doi:10.1016/j.molstruc.2010.08.006

Freundlich, H. (1907). Über die Adsorption in Lösungen. *Z. Phys. Chem.* 57U, 385–470. doi:10.1515/zpch-1907-5723

Guo, D., Zhu, L., Guo, S., Cui, B., Luo, S., Laghari, M., et al. (2016). Direct Reduction of Oxidized Iron Ore Pellets Using Biomass Syngas as the Reducer. *Fuel Process. Tech.* 148, 276–281. doi:10.1016/j.fuproc.2016.03.009

Guz, L., Curutchet, G., Torres Sánchez, R. M., and Candal, R. (2014). Adsorption of crystal Violet on Montmorillonite (Or Iron Modified Montmorillonite) Followed by Degradation through Fenton or Photo-Fenton Type Reactions. *J. Environ. Chem. Eng.* 2, 2344–2351. doi:10.1016/j.jece.2014.02.007

Hammed, A. K., Dewayanto, N., Du, D., Ab Rahim, M. H., and Nordin, M. R. (2016). Novel Modified ZSM-5 as an Efficient Adsorbent for Methylene Blue Removal. *J. Environ. Chem. Eng.* 4, 2607–2616. doi:10.1016/j.jece.2016.05.008

Ho, Y. S., and McKay, G. (1999). Pseudo-second Order Model for Sorption Processes. *Process Biochem.* 34, 451–465. doi:10.1016/S0032-9592(98)00112-5

Int, C., Iqbal, M., Nisar, J., Nazir, A., and Qamar, A. Z. (2019). Bioassays Based on Higher Plants as Excellent Dosimeters for Ecotoxicity Monitoring: a Review. *Chem. Int.* 5, 1–80. doi:10.31221/osf.io/z2ynm

Kerkez, D. V., Tomašević, D. D., Kozma, G., Bečelić-Tomin, M. R., Prica, M. D., Rončević, S. D., et al. (2014). Three Different clay-supported Nanoscale Zero-Valent Iron Materials for Industrial Azo Dye Degradation: a Comparative Study. *J. Taiwan Inst. Chem. Eng.* 45, 2451–2461. doi:10.1016/j.jtice.2014.04.019

Lagergren, S. (1898). Zur theorie der sogenannten adsorption gelöster stoffe, Kungliga Svenska Vetenskapsakademiens. *Handl* 24, 1–39.

Langmuir, I. (1918). The Adsorption of Gases on Plane Surfaces of Glass, Mica and Platinum. *J. Am. Chem. Soc.* 40, 1361–1403. doi:10.1021/ja02242a004

Li, Z., Chen, Z., Zhu, Q., Song, J., Li, S., and Liu, X. (2020). Improved Performance of Immobilized Laccase on Fe3O4@C-Cu2+ Nanoparticles and its Application for Biodegradation of Dyes. *J. Hazard. Mater.* 399, 123088. doi:10.1016/j.jhazmat.2020.123088

Liu, J., Wang, Y., Fang, Y., Mwamulima, T., Song, S., and Peng, C. (2018). Removal of crystal Violet and Methylene Blue from Aqueous Solutions Using the Fly Ash-Based Adsorbent Material-Supported Zero-Valent Iron. *J. Mol. Liquids* 250, 468–476. doi:10.1016/j.molliq.2017.12.003

Liu, S., Lim, M., and Amal, R. (2014). TiO2-coated Natural Zeolite: Rapid Humic Acid Adsorption and Effective Photocatalytic Regeneration. *Chem. Eng. Sci.* 105, 46–52. doi:10.1016/j.ces.2013.10.041

Liu, Y., Phenrat, T., and Lowry, G. V. (2007). Effect of TCE Concentration and Dissolved Groundwater Solutes on NZVI-Promoted TCE Dechlorination and H2 Evolution. *Environ. Sci. Technol.* 41, 7881–7887. doi:10.1021/es0711967

Man, Y., Feng, J. X., Li, F. J., Ge, Q., Chen, Y. M., and Zhou, J. Z. (2014). Influence of Temperature and Time on Reduction Behavior in Iron Ore-Coal Composite Pellets. *Powder Tech.* 256, 361–366. doi:10.1016/j.powtec.2014.02.039

Mishra, P., Singh, K., and Dixit, U. (2021). Adsorption, Kinetics and Thermodynamics of Phenol Removal by Ultrasound-Assisted Sulfuric Acid-Treated Pea (Pisum Sativum) Shells. *Sust. Chem. Pharm.* 22, 100491. doi:10.1016/j.scp.2021.100491

Mwamulima, T., Zhang, X., Wang, Y., Song, S., and Peng, C. (2018). Novel Approach to Control Adsorbent Aggregation: Iron Fixed Bentonite-Fly Ash for Lead (Pb) and Cadmium (Cd) Removal from Aqueous media. *Front. Environ. Sci. Eng.* 12, 2. doi:10.1007/s11783-017-0979-6

Ngulube, T., Gumbo, J. R., Masindi, V., and Maity, A. (2019). Preparation and Characterisation of High Performing Magnesite-Halloysite Nanocomposite and its Application in the Removal of Methylene Blue Dye. *J. Mol. Struct.* 1184, 389–399. doi:10.1016/j.molstruc.2019.02.043

Nourein, S., Bhatti, H., Iqbal, M., Bibi, I., Zafar, N., Iqbal, D., et al. (2017). Redox Mediators Assisted-Degradation of Direct Yellow 4. *Pol. J. Environ. Stud.* 26, 2885–2890. doi:10.15244/pjoes/68564

Ramamoorthy, M., Ragupathy, S., Sakthi, D., Arun, V., and Kannadasan, N. (2020). Synthesis of SnO2 Loaded on Corn Cob Activated Carbon for Enhancing the Photodegradation of Methylene Blue under Sunlight Irradiation. *J. Environ. Chem. Eng.* 8, 104331. doi:10.1016/j.jece.2020.104331

Rasalingam, S., Peng, R., and Koodali, R. T. (2015). An Insight into the Adsorption and Photocatalytic Degradation of Rhodamine B in Periodic Mesoporous Materials. *Appl. Catal. B: Environ.* 174-175, 49–59. doi:10.1016/j.apcatb.2015.02.040

Saber-Samandari, S., Saber-Samandari, S., Joneidi-Yekta, H., and Mohseni, M. (2017). Adsorption of Anionic and Cationic Dyes from Aqueous Solution Using Gelatin-Based Magnetic Nanocomposite Beads Comprising Carboxylic Acid Functionalized Carbon Nanotube. *Chem. Eng. J.* 308, 1133–1144. doi:10.1016/j.cej.2016.10.017

Spadaro, J. T., Gold, M. H., and Renganathan, V. (1992). Degradation of Azo Dyes by the Lignin-Degrading Fungus Phanerochaete Chrysosporium. *Appl. Environ. Microbiol.* 58, 2397–2401. doi:10.1016/1050-1738(93)90025-210.1128/aem.58.8.2397-2401.1992

Stephen Inbaraj, B., and Chen, B. H. (2011). Dye Adsorption Characteristics of Magnetite Nanoparticles Coated with a Biopolymer Poly(γ-Glutamic Acid). *Bioresour. Tech.* 102, 8868–8876. doi:10.1016/j.biortech.2011.06.079

Wang, J.-Q., Liu, Y.-H., Chen, M.-W., Xie, G.-Q., Louzguine-Luzgin, D. V., Inoue, A., et al. (2012). Rapid Degradation of Azo Dye by Fe-Based Metallic Glass Powder. *Adv. Funct. Mater.* 22, 2567–2570. doi:10.1002/adfm.201103015

Wang, W., Cheng, Y., Kong, T., and Cheng, G. (2015). Iron Nanoparticles Decoration onto Three-Dimensional Graphene for Rapid and Efficient Degradation of Azo Dye. *J. Hazard. Mater.* 299, 50–58. doi:10.1016/j.jhazmat.2015.06.010

Wang, Y., López-Valdivieso, A., Zhang, T., Mwamulima, T., Zhang, X., Song, S., et al. (2017). Preparation of Microscale Zero-Valent Iron-Fly Ash-Bentonite Composite and Evaluation of its Adsorption Performance of crystal Violet and Methylene Blue Dyes. *Environ. Sci. Pollut. Res.* 24, 20050–20062. doi:10.1007/s11356-017-9426-2

Weber, W. J., and Morris, J. C. (1963). Kinetics of Adsorption on Carbon from Solution. *J. Sanit. Engrg. Div.* 89, 31–59. doi:10.1061/JSEDAI.0000430

Xu, C.-H., Zhu, L.-j., Wang, X.-H., Lin, S., and Chen, Y.-m. (2014). Fast and Highly Efficient Removal of Chromate from Aqueous Solution Using Nanoscale Zero-Valent Iron/activated Carbon (nZVI/AC). *Water Air Soil Pollut.* 225, 1845. doi:10.1007/s11270-013-1845-1

Xu, H.-M., Sun, X.-F., Wang, S.-Y., Song, C., and Wang, S.-G. (2018). Development of Laccase/graphene Oxide Membrane for Enhanced Synthetic Dyes Separation and Degradation. *Sep. Purif. Tech.* 204, 255–260. doi:10.1016/j.seppur.2018.04.036

Zhang, J., Zhang, T., Liang, X., Wang, Y., Shi, Y., Guan, W., et al. (2020a). Efficient Photocatalysis of CrVI and Methylene Blue by Dispersive Palygorskite-Loaded Zero-Valent Iron/carbon Nitride. *Appl. Clay Sci.* 198, 105817. doi:10.1016/j.clay.2020.105817

Zhang, L., Yao, L., Ye, L., Long, B., Dai, Y., and Ding, Y. (2020b). Benzimidazole-based Hyper-Cross-Linked Polymers for Effective Adsorption of Chlortetracycline from Aqueous Solution. *J. Environ. Chem. Eng.* 8, 104562. doi:10.1016/j.jece.2020.104562

Zhang, X., Lin, S., Lu, X.-Q., and Chen, Z.-l. (2010). Removal of Pb(II) from Water Using Synthesized Kaolin Supported Nanoscale Zero-Valent Iron. *Chem. Eng. J.* 163, 243–248. doi:10.1016/j.cej.2010.07.056

Zheng, Q., Zhang, Z. R., Du, J., Lin, L. L., Xia, W. X., Zhang, J., et al. (2019). A Novel Direct Reduction Method to Synthesize Ordered Fe-Pt alloy Nanoparticles. *J. Mater. Sci. Tech.* 35, 560–567. doi:10.1016/j.jmst.2018.09.036

Conflict of Interest: The authors declare that the research was conducted in the absence of any commercial or financial relationships that could be construed as a potential conflict of interest.

Publisher's Note: All claims expressed in this article are solely those of the authors and do not necessarily represent those of their affiliated organizations, or those of the publisher, the editors, and the reviewers. Any product that may be evaluated in this article, or claim that may be made by its manufacturer, is not guaranteed or endorsed by the publisher.